Δελτίο της Ελληνικής Γεωλογικής Εταιρίας, τόμος L, σελ. 1583-1592
Πρακτικά 14ου Διεθνούς Συνεδρίου, Θεσσαλονίκη, Μάιος 2016

Bulletin of the Geological Society of Greece, vol. L, p. 1583-1592
Proceedings of the 14th International Congress, Thessaloniki, May 2016

THE 2014 M_W 6.9 NORTH AEGEAN TROUGH (NAT) EARTHQUAKE: SEISMOLOGICAL AND GEODETIC EVIDENCE

Saltogianni V.[1], Gianniou M.[2], Taymaz T.[3], Yolsal-Çevikbilen S.[3] and Stiros S.[1]

[1]Department of Civil Engineering, University of Patras, Patras, Greece
vsalt@upatras.gr, stiros@upatras.gr

[2]National Cadastre and Mapping Agency SA, Athens, Greece
mgianniu@ktimatologio.gr

[3]Department of Geophysical Engineering, The Faculty of Mines, İstanbul Technical University, İstanbul, Turkey, taymaz@itu.edu.tr, yolsalse@itu.edu.tr

Abstract

A strong earthquake (Mw 6.9) on 24 May 2014 ruptured the North Aegean Trough (NAT) in Greece, west of the North Anatolian Fault Zone (NAFZ). In order to provide unbiased constrains of the rupture process and fault geometry of the earthquake, seismological and geodetic data were analyzed independently.
First, based on teleseismic long-period P- and SH- waveforms a point-source solution yielded dominantly right-lateral strike-slip faulting mechanism. Furthermore, finite fault inversion of broad-band data revealed the slip history of the earthquake.
Second, GPS slip vectors derived from 11 permanent GPS stations uniformly distributed around the meizoseismal area of the earthquake indicated significant horizontal co-seismic slip. Inversion of GPS-derived displacements on the basis of Okada model and using the new TOPological INVersion (TOPINV) algorithm permitted to model a vertical strike slip fault, consistent with that derived from seismological data.
Obtained results are consistent with the NAT structure and constrain well the fault geometry and the dynamics of the 2014 earthquake. The latter seems to fill a gap in seismicity along the NAT in the last 50 years, but seems not to have a direct relationship with the sequence of recent faulting farther east, along the NAFZ.
Keywords: *focal mechanism, active tectonics, surface deformation, Samothraki, Gökçeada (Imvros).*

1. Introduction

On 24 May 2014, a strong and shallow earthquake (Mw 6.9, focal depth: 11km), occurred in the North Aegean Sea, between the islands of Samothraki, Gökceada (Imvros) and Limnos (Figure 1). The 2014 earthquake is the largest event in the last 50 years recorded along the North Aegean Trough (NAT; Taymaz *et al*., 1991), which is hosted in this area. The NAT is a 300km-long system of marine basins, up to 1000m deep, representing the western extension of the North Anatolian Fault Zone (NAFZ; Figure 1; Le Pichon *et al*., 1987; Taymaz *et al.*, 1991; Karabulut *et al*., 2003; Reilinger *et al*., 2010 and Müller *et al*., 2013). Tectonics along the NAT are active, as historical and recent seismicity reveal (Papazachos and Papazachou, 1997 and Taymaz and Yolsal-Çevikbilen, 2015). The analysis of recent seismic sequences indicates strike-slip faulting (Taymaz and Yolsal-Çevikbilen, 2015), while geodetic data indicate that the NAT corresponds to a major strike-slip fault

with an average slip rate of the order of 20mm/yr (Reilinger *et al*., 2010). Although earthquakes with magnitude M > 6.5 are supposed to produce major damage in a broader region (Papazachos and Papazachou, 1997), the 2014 earthquake produced low accelerations even in the near-field (maximum peak 0.11g; ITSAK, 2014; KOERI, 2014), and therefore only minor damage was observed. However, it led to some term of panic in the Çanakkale and İstanbul areas, since a possible forthcoming earthquake is expected in the west of the 1999 Kocaeli-İzmit rupture, as a continuation of the westward migrating large earthquakes along the NAFZ since 1939 (Ergintav *et al*., 2009).

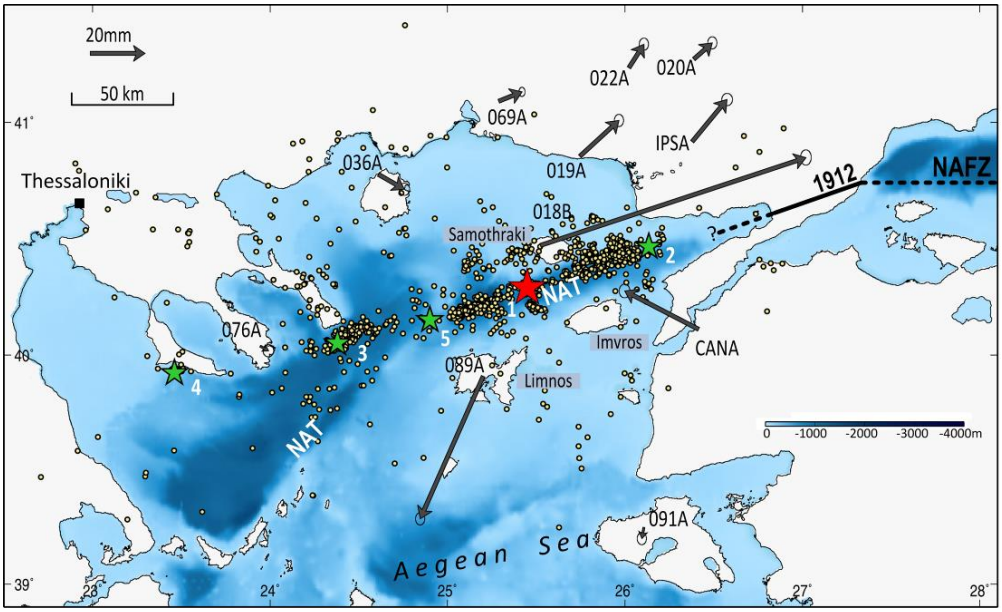

Figure 1 – The NAT (noticeable by bathymetry) at the continuation of NAFZ and the epicenter of the 2014 earthquake (red star). Green stars 2-5 indicate main events (numbered based on time occurrence) in the seismic sequence from 24 May to 5 September 2014 and yellow circles denote smaller events forming the five clusters (events were relocated by Evangelidis, 2014, for longitude<23.7 events were derived from the relocated catalogue of NOA, 2014). GPS-derived displacements (black arrows) are also shown with 3-σ error ellipses.

The distribution of the aftershocks after the main event (Evangelidis, 2014; NOA, 2014) revealed five clusters of aftershocks (Figure 1) which correlate with the NAT and seem to cover its major part. The only exception is "cluster 4" which appears somewhat distant from the NAT. One characteristic of the seismic sequence is the considerable spread of the zone of aftershocks, extending up to 180km (or even 250km if cluster "4" is included in the seismic sequence). Strong motion recordings suggest that the main shock consisted of two distinct events, separated by a time interval of about ~10s (ITSAK, 2014), while a further study of strong motion data by Evangelidis (2014) concluded that the seismic sequence consisted of two distinct events separated by a 13s interval; the first one correlates with the epicentre, while the second one is characterized by super-shear rupture.

This article is based on the independent inversion and joint interpretation of teleseismic waveforms and of GPS co-seismic slip vectors permitting to model in detail the rupture geometry and dynamics of the 2014 earthquake. Because the seismological networks in the wider study area are rather limited, this study is useful to understand the active tectonics along NAT and its possible relationship with faulting along the NAFZ, characterized by a westwards propagation of earthquakes since 1939.

2. Inversion of Seismological Data

2.1. Seismic waveform inversion for source parameters

The point-source inversion is performed to obtain source parameters of the NAT earthquake (strike, dip, rake angles, focal depth, seismic moment and source time functions) using teleseismic ($30° \leq \Delta \leq 90°$) long-period P- and SH- waveforms and first motion polarities of P-waves which are provided by the Federation of Digital Seismograph Networks (FDSN) and the Global Digital Seismograph Network (GDSN). We used MT5 (Moment Tensor 5) body-waveform inversion algorithm (Zwick *et al*., 1994). In the inversion, we used a half-space source velocity model, a simplified crustal model, consisting of P-wave velocity (Vp) = 6.8 km/s, S-wave velocity (Vs) = 3.9 km/s and density (ρ) = 2.9 g/cm^3. Based on bathymetry data, we defined a water layer with a velocity of Vp = 1.5 km/s and varying thicknesses (~ 0.5-1 km). The medium below the receivers are assumed to be homogeneous half-spaces.

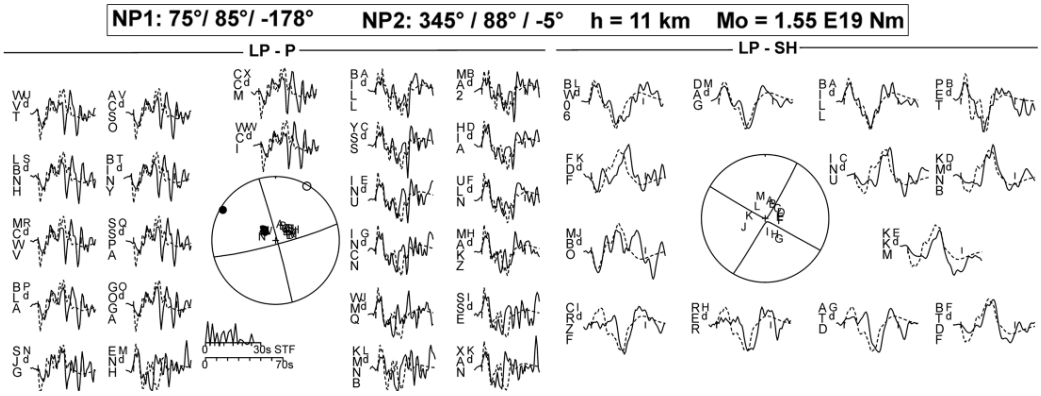

Figure 2 - The radiation patterns and synthetic waveform fits for the minimum misfit solution determined by using the inversion of teleseismic long-period 24 P- and 13 SH-waveforms of the May 24, 2014 Samothraki-Gökçeada earthquake. Solid and dashed lines are observed and synthetic waveforms, respectively.

A set of acceptable point-source parameters of the 2014 earthquake was obtained (strike: 75°, dip: 85°, rake: -178°, depth: 11 km and M_0: 1.55x1019 Nm; see Figure 2). Our best-fitting waveform point-source solution yielded dominantly right-lateral strike-slip faulting mechanism, which is consistent with the morphology of the NAT and the NAFZ and preliminary focal mechanisms (KOERI, 2014; NOA, 2014). Focal depth is shallow (h: 11km) and the source duration is relatively long (~30s) in comparison to earthquakes of similar size. The slip vector at the hypocenter plunges at 2° towards 75°. Furthermore, we estimated the uncertainties of strike, dip, rake, and depth by investigating one parameter at a time. Fixing each parameter at a series of values on either side of the value, yielded by the minimum misfit solution and allowing the other parameters to be estimated by the inversion routine, we obtained that the error bounds for strike, dip and rake angles and the focal depth are within the range of ± 5°, and ± 2 km, respectively.

2.2. Finite-fault slip modelling

Teleseismic broad-band P-waveforms were windowed for 60s, starting 10s before the origin time. After band-pass filtering between 0.01 Hz and 0.8 Hz, velocity seismograms were converted into ground displacement with a sampling rate of 0.2s. The earthquake source model is constructed using a standard waveform inversion scheme given by Hartzell and Heaton (1983). The basic assumption is that faulting occurs on a single fault plane, and slip angle remains unchanged during the whole rupture process. Further details of finite-fault slip inversion can be found at relevant studies (Yagi and Kikuchi, 2000 and Fielding *et al*., 2013). The fault plane was fixed to the best fitting point-source solution. The rupture front velocity (Vr) was set as 3.2 km/s. The rake angle was fixed at -

178° as obtained from the point source solution. The source-time (slip-rate) function of each sub-fault was expanded in a series of overlapping triangles of source time functions each with a rise time of 1.25 s. Several trials were made with different number of cells, cell-sizes, epicentre location, number of triangles function and number of seismic stations in order to find the optimum solution. The latter corresponded to a fault plane of 25x10 sub-faults with dimensions of 2.5x2.5km^2 which were expanded in a series of 15 triangle functions. The best finite-fault slip distribution obtained is shown in Figure 3 and the observed and synthetic waveforms in Figure 4.

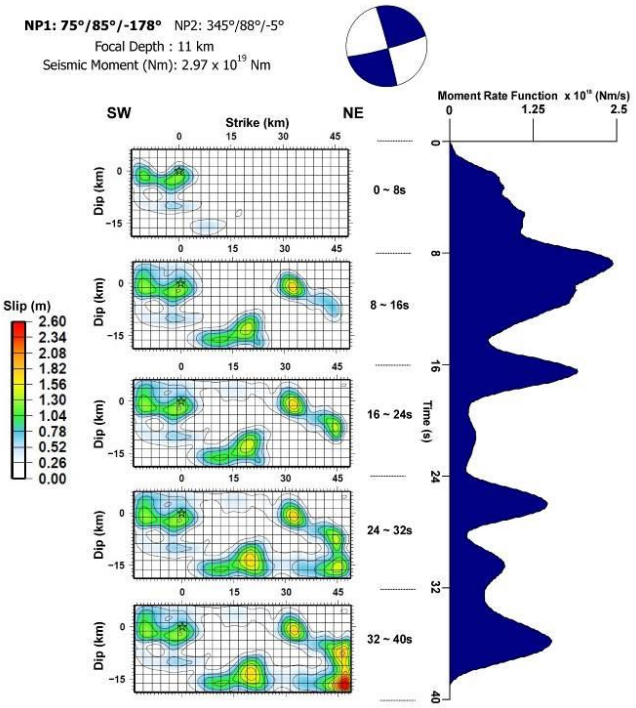

Figure 3 - Focal mechanism, finite-fault slip distribution, and total moment rate function of the 2014 NAT earthquake in time. Slip model was derived on NP1 and a star indicates location of the hypocentre.

The results indicate that the initial fragment of the slip occurred in close vicinity to the hypocentre (~100-150 cm). Our preferred finite-fault model has areas of strong slip (~150 cm) in the centre and in the northeast segments, deeper than the hypocentre. However, the maximum displacement (~ 260 cm) observed at east edge of the plane may be an artefact as it was not evident in all trials (Figure 3). The slip model shows that rupture propagated along mainly the strike direction of the fault from SW to NE with a slip-vector of 75º. The waveform fits matches well at all azimuths, and indicative of late moment release seen beyond ~13 s reaching maximum level of displacement which is exceptionally consistent with reported results of strong motion by Evangelidis (2014). We found that the total moment of the finite-fault model is 2.97x10^{19} Nm; i.e. Mw 6.9. The fault length and width of the fault plane were determined as 62.5km and 25km, respectively with an average slip of 63cm.

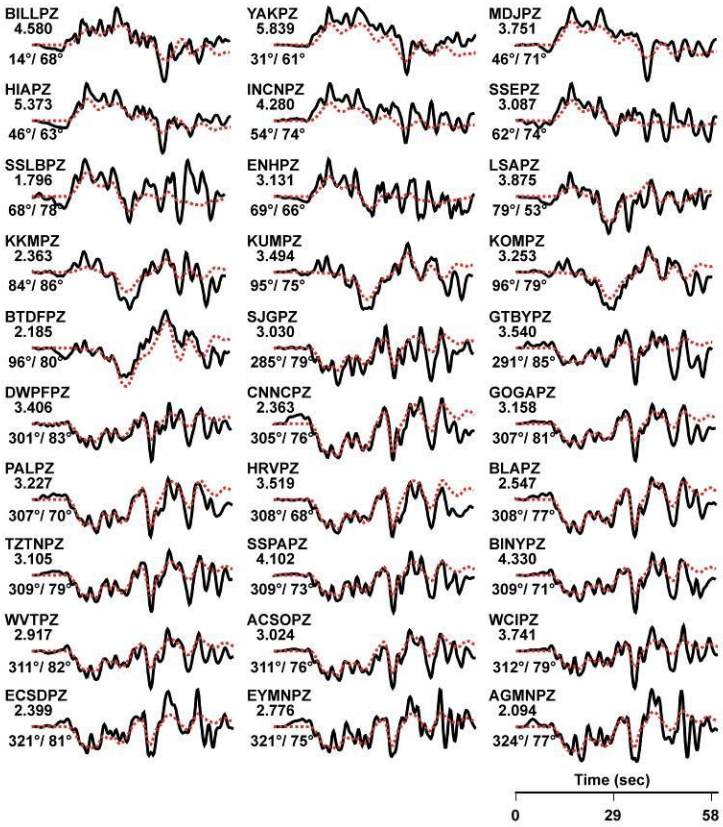

Figure 4 - Comparison of the observed (solid black line) and synthetic (dashed red line) broadband P waveforms.

3. Inversion of Geodetic Data

3.1. Data and analysis

We used data from 11 permanent GPS stations around the earthquake area for the period between 2014.05.10 and 2014.06.07; consisting of two intervals of 14 days before and after the day of the earthquake. These stations belong to the HEllenic POsitioning System (HEPOS), except for two stations (CANA and IPSA) which belong to the Turkish National Fundamental GPS Network (TUTGA). The locations of the GPS stations are shown in Figure 1. The distribution is nearly uniform around the epicentral area and it covers both near and far field stations. The datasets used are daily records with 30s sampling interval. Each station was analysed independently using Precise Point Positioning (PPP; Zumberge *et al*., 1997) and the GrafNav software ver. 8.40 to compute mean daily geographic coordinates for each station, and then mean pre- and post-seismic coordinates and their uncertainties. Horizontal displacements for all the stations are shown in Figure 1. In contrast to horizontal displacements, no statistically significant and consistent vertical displacements were found, including stations 089A and 018B in close proximity to the epicentral area. This result was confirmed by processing the same dataset using a baseline adjustment technique.

3.2. Inversion methodology for GPS data-the TOPINV algorithm

The geophysical problem is described by the Okada (1985) equations which express GPS measurements of m surface displacement as functions of n=9 unknown variables describing the geometry and slip of a single rectangular fault with uniform slip in an elastic half-space ($\boldsymbol{x}$: fault

centre, depth of the upper tip, length, width, dip, strike, rake and slip). These equations lead to a redundant system of m highly-non-linear equations with n unknowns of the form (1)

$$f(\boldsymbol{x}) = \boldsymbol{l} + \boldsymbol{u} \quad (1)$$

with $\boldsymbol{u}$ unknown errors assumed random with standard deviation $\boldsymbol{\sigma}$.

Using the new TOPological INVersion (TOPINV) algorithm a priori independent conditions (mostly seismological and geological) have to be defined; i.e. the possible ranges of the variables $\boldsymbol{x}$. Discretization of each of the n variables leads to a hyper-grid G in the R^n space. Introducing a scale factor $k>0$, observation equations (1) yield into a system of inequalities

$$\left| f(\boldsymbol{x}) - \boldsymbol{l} \right| \le k\,\boldsymbol{\sigma} \quad (2)$$

Then, for a selected value of k all grid-points in G are tested using a Boolean logic whether they satisfy inequalities (2) and successful points are identified, defining sets S. After repeated trials for different values of k, an optimal k^* is obtained. The latter leads to a set S^* of grid-points that have a certain distribution (closed space) and the optimal solution and its variance-covariance matrix are estimated as the first and second statistical moments of this set. Apparently, the solution depends on the geophysical model selected, the observations and their uncertainties, as well a priori conditions of the hyper-grid G. The algorithm does not focus on point solutions or local minima, or on solutions at the vicinity of specific points. The main limitation of this algorithm is the large number of grid-points, which for common computers should be up to the order of 10^{10} to avoid excessive computing load. To overpass this problem, a coarser grid is first used leading to one or more coarser solutions. Then we adopted nested grids, with finer spacing leading to more accurate solutions. The details of this algorithm are described in more detail in Saltogianni and Stiros (2012, 2015) and Saltogianni *et al*. (2014).

3.3. Results

At a first step, a Grid G^1 in a discretized R^9 space covering all possible values of the unknown variables defining the seismic fault was defined on the basis of the available seismological data. The centre of the fault was allowed to be anywhere in a wide 2-D rectangular (Figure 5) around the epicentre. The strike, dip and rake angles of the fault were also allowed to cover a range of 60-90^o, 75-90^o, 170-190^o, respectively. The upper tip of the fault was allowed to range from the surface (d=0) to d=15km, and because of the selected width range (10-40km) its lower limit was allowed to reach the depth of 55km. The length of the fault was allowed to cover any possibility for a fault of this magnitude, i.e. between 30-70km. Given that the maximum slip recorded at station 018B at a distance of ~20km away from the epicentre was about 10cm, a range between 20-90cm was assumed for the slip (Wells and Coppersmith, 1994). For each variable an appropriate spacing was selected so that the total number of gridpoints of Grid G^1 does not exceed the limit of 10^{10}. A flat weight of 0.6mm was adopted for observations in Easting and 0.8mm for Northing, based on the estimated standard deviations of the displacements.

All the above were used as inputs in the inequalities (2) and computations started using a first value of k=1, but no solution for this value was available. So the computations were repeated for gradually increased values, until the value k^1=12, which corresponds to a cluster of points S^1 consisting of ~100 gridpoints in total. The overall process was then repeated for a nested Grid G^2 containing S^1 but with a finer spacing, until a solution was obtained for k^*=10.5. This solution corresponds to a cluster of ~60 points. At a final step we computed the centre of gravity of this cluster and the uncertainty of each of the values of the 9 variables defining the fault. This solution was accepted as final (optimal) because the uncertainties of the fault variables are small and the misfit between GPS observations and predictions of displacements is nearly optimal χ^2_ν = 5.37. The obtained results (Figure 5) correspond to an essentially vertical strike-slip fault, ~ 60km long, cutting from the seabed to the depth of ~20km, with a strike of ~80^o, correlating with the NAT and with a mean slip of ~70cm and seismic moment of 2.4 x10^{19}Nm.

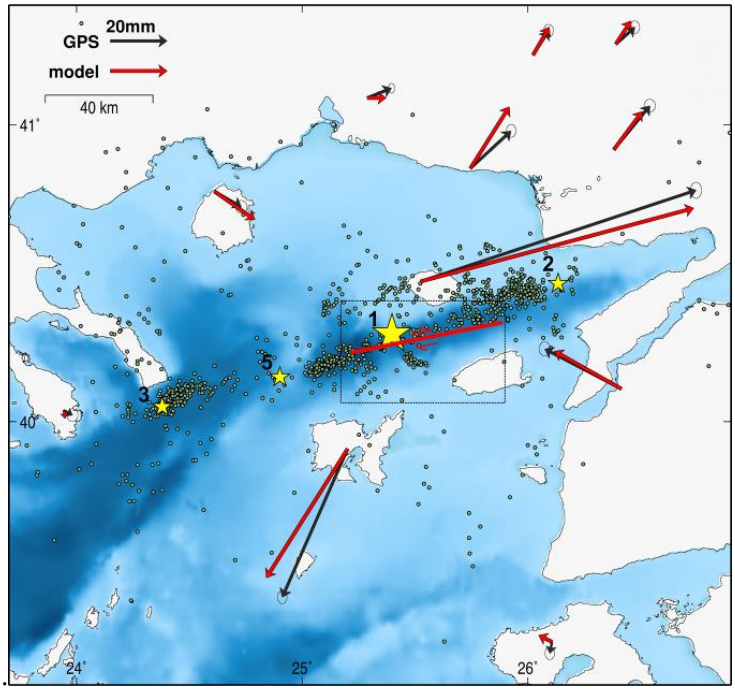

Figure 5 – GPS-derived and modelled displacements (black and red arrows, respectively). The projection of the modelled fault is indicated by a red line. Aftershock clusters and main events (yellow stars) in each cluster are also shown (see Figure 1). A rectangular denotes the search area of the centre of the fault.

4. Discussion and Conclusions

4.1. Comparison and assessment of the models

The geometry and dynamics of the 2014 NAT earthquake have been analysed on the basis of independent inversion of two different datasets, seismological and geodetic. Fitting is very good for both the seismological and the geodetic data, while the corresponding fault-models of a vertical strike-slip fault are fully consistent to each other and with preliminary focal mechanisms and with local tectonics.

The overall conclusion of the analysis of the two datasets, is that the 2014 earthquake was associated with a nearly pure right-lateral strike-slip fault of about ~60km long, reaching from the seabed to a depth of ~20km with an average slip of ~70cm. The computed seismic moment is 2.4-3.0 $x10^{19}$Nm, corresponding to an earthquake of magnitude 6.9.

The reason that differences are observed in the two models (dip, strike) could be because the geodetic model describes an average fault fitting observations of surface deformation, while point source solutions are rather indicative of instantaneous rupture effects.

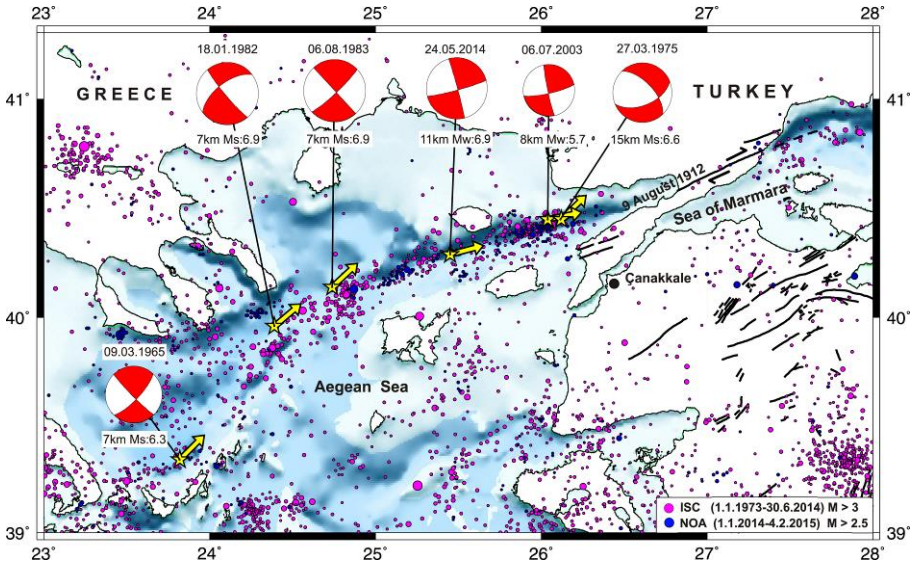

Figure 6 – Location and focal mechanisms of the largest earthquakes in NAT area the last 50 years (Taymaz *et al.*, 1991; Taymaz and Yolsal-Çevikbilen, 2015). Yellow arrows indicate slip-vectors of earthquakes. The 24 May 2014 earthquake sequence seems to fill a gap in seismicity in the NAT between 1965 and 2014.

4.2. Seismotectonic implications

In the context of the previous analysis, three points need to be discussed.

First, evidence from accelerograms indicates a main shock comprising two sub-events (ITSAK, 2014), as well as the analysis of strong motion data of Evangelidis (2014) indicates a complex fault pattern, comprising two faults, associated with the two distinct clusters of aftershocks 1 and 2 (Figure 1), with the second fault associated with supershear rupture. Although, the single fault pattern obtained from geodetic data (Figure 5) describes well the data, further analysis assuming a two-fault pattern is in progress and will be presented elsewhere.

Second, the 2014 earthquake was of a magnitude usually producing extensive damage in the region, but its damaging effects were actually very limited. Such an earthquake in the past would have passed practically unnoticed. Given that historical earthquakes in the region were recorded in ancient texts in a few main cultural centres (Athos Monasteries at the SE edge of the Chalkidiki Peninsula, Thessaloniki and Istanbul), it is quite possible that many strong historical earthquakes which produced moderate strong motion were ignored and not included in the historical seismicity catalogues (Papazachos and Papazachou, 1997); a result supported by recent independent evidence concerning the tectonics of the Strymon Fault (Mouslopoulou *et al.*, 2014).

Third, a major problem is the relationship of the 2014 earthquake to other earthquakes in the NAT, as well as in the NAFZ. Figure 6 summarizes the focal mechanisms of the largest earthquakes in the North Aegean in the last 50 years. Interestingly, in the Aegean Sea, at the west continuation of the NAFZ, the sequence of faults and earthquakes seems not to be characterized by a gradual progression in one direction. In the central and eastern Aegean, and NW Turkey, distributed right-lateral strike-slip is more prevalent on faults trending NE to E-NE and with slip vectors directed to NE (Taymaz *et al.*, 1991). Fault plane solutions in the NAT show mainly strike-slip faulting, consistent with right-lateral slip on NE-SW striking faults. The-strike slip faulting that enters the central Aegean from the east (the 1912 NAFZ fault, Aksoy *et al.*, 2010) appears to end abruptly in the SW against the NW coasts of continental Greece (Figures 1, 6), marked by Quaternary coastal uplifts (Stiros *et al.*, 1994). Hence from the examination of Figure 6 showing major earthquakes along the NAT, it is evident that no oriented progress of seismic faulting, coupled with that observed

along the NAFZ in the last 50 years exists. On the contrary, the 2014 earthquake seems to have filled a gap in seismic faulting since 1965 in the NAT, west of the 1912 fault.

5. Acknowledgments

We thank the National Cadastre and Mapping Agency of Greece for granting permission to publish results of the analysis of data from the HEPOS network. VS was partly supported by a project funded by the Greek Secretariat of Research and Technology, Greece. TT thanks İstanbul Technical University Research Fund, Turkish National Scientific and Technological Foundation, Turkish Academy of Sciences in the framework for Young Scientist Award Program and Alexander von Humboldt-Foundation.

6. References

Aksoy, M.E., Meghraoui, M., Vallée, M. and Çakır, Z., 2010. Rupture characteristics of the A.D. 1912 Mürefte (Ganos) earthquake segment of the North Anatolian fault (western Turkey), *Geology*, 38(11), 991-994.

Ergintav, S., McClusky, S., Hearn, E., Reilinger, R., Cakmak, R., Herring, T., Ozener, H., Lenk, O. and Tari, E., 2009. Seven years of postseismic deformation following the 1999, M = 7.4 and M = 7.2, Izmit-Duzce, Turkey earthquake sequence, *J. Geophys. Res.*, 114, B07403.

Evangelidis, C.P., 2014. Imaging supershear rupture for the 2014 Mw 6.9 Northern Aegean earthquake by backprojection of strong motion waveforms, *Geophys. Res. Lett*., 2014GL062513.

Fielding, E.J., Lundgren, P.R., Taymaz, T., Yolsal-Çevikbilen, S. and Owen, S.E., 2013. Fault-Slip Source Models for the 2011 M 7.1 Van Earthquake in Turkey from SAR Interferometry, Pixel Offset Tracking, GPS, and Seismic Waveform Analysis, *Seismological Research Letters*, 84(4), 579-593.

Hartzell, S.H. and Heaton, T.H., 1983. Inversion of strong ground motion and teleseismic waveform data for the fault rupture history of the 1979 Imperial Valley, California, earthquake, *Bulletin of the Seismological Society of America*, 73(6), 1553-1583.

ITSAK, 2014. Institute of Engineering Seismology and Earthquake Engineering of Greece, http://www.itsak.gr/db/data/sm/after2000.

Karabulut, H., Roumelioti, Z., Benetatos, C., Multu, A.K., Özalaybey, S., Aktar, M. and Kiratzi, A., 2006. A source study of the 6 July 2003 (Mw 5.7) earthquake sequence in the Gulf of Saros (Northern Aegean Sea): Seismological evidence for the western continuation of the Ganos fault, *Tectonophysics*, 412(3-4), 195-216.

KOERI, 2014. Earthquake Report of 24 May 2014 Northern Aegean Sea, Tech. Rep., Kandilli Observatory and Earthquake Research Institute, Boğaziçi Univ, Istanbul, Turkey.

Le Pichon, X., Lybéris, N. and Alvarez, F., 1987. Discussion on the subsidence of the North Aegean trough: an alternative view, *Journal of the Geological Society*, 144(2).

Mouslopoulou, V., Saltogianni, V., Gianniou, M. and Stiros, S., 2014. Geodetic evidence for tectonic activity on the Strymon Fault System, northeast Greece, *Tectonophysics*, 633, 246-255.

Müller, M.D., Geiger, A., Kahle, H.-G., Veis, G., Billiris, H., Paradissis, D. and Felekis, S., 2013.Velocity and deformation fields in the North Aegean domain, Greece, and implications for fault kinematics, derived from GPS data 1993-2009, *Tectonophysics*, 597-598, 34-49.

NOA, 2014. National Observatory of Athens, Greece. http://bbnet.gein.noa.gr/HL/.

Okada, Y., 1985. Surface deformation due to shear and tensile faults in a half-space, *Bulletin of the Seismological Society of America*, 75(4), 1135-1154.

Papazachos, B. and Papazachou, C., 1997. The Earthquakes of Greece. P. Ziti and Co, Thessaloniki, Greece, 304 pp.

Reilinger, R., McClusky, S., Paradissis, D., Ergintav, S. and Vernant, P., 2010. Geodetic constraints on the tectonic evolution of the Aegean region and strain accumulation along the Hellenic subduction zone, *Tectonophysics*, 488(1-4).

Saltogianni, V. and Stiros, S., 2012. Adjustment of highly non-linear redundant systems of equations using a numerical, topology-based approach, *Journal of Applied Geodesy*, 6(3-4), 125-134.

Saltogianni, V. and Stiros S., 2015. A two-fault model of the 2003 Leucas (Aegean Arc) earthquake based on topological inversion of GPS data, *Bulletin of the Seismological Society of America*, 105(5), 2510-2520.

Saltogianni, V., Stiros, S.C., Newman, A.V., Flanagan, K. and Moschas F., 2014. Time-space modeling of the dynamics of Santorini volcano (Greece) during the 2011-2012 unrest, *J. Geophys. Res. Solid Earth*, 2014JB011409.

Stiros, S., Pirazzoli, P., Pomoni-Papaioannou, F., Laborel, J., Laborel, F. and Arnold, M., 1994. Late Quaternary uplift of the Olympus-Pelion Range (Macedonia-Thessaly, Greece), *Bull. Geol. Soc Greece*, 30 Jan 1994, 325-330.

Taymaz, T., Jackson, J. and McKenzie, D., 1991. Active tectonics of the north and central Aegean Sea, *Geophys. J. Int.*, 106(2), 433-490.

Taymaz, T. and Yolsal-Çevikbilen, S., 2015. Source Parameters of Major Earthquakes in the Aegean during 2013-2014: Implications on Recent Tectonics and Deformations, Geophysical Research Abstracts, Vol. 17, EGU2015-4744, 12-17 April 2015, Vienna, Austria.

Wells, D.L. and Coppersmith K.J., 1994. New empirical relationships among magnitude, rupture length, rupture width, rupture area, and surface displacement, *Bull. Seismol. Soc. Am.*, 84(4), 974-1002.

Yagi, Y. and Kikuchi, M., 2000. Source rupture process of the Kocaeli, Turkey, earthquake of August 17, 1999, obtained by joint inversion of near-field data and teleseismic data, *Geophys. Res. Lett.*, 27(13), 1969-1972.

Zumberge, J.F., Heflin, M.B., Jefferson, D.C., Watkins, M.M. and Webb F.H., 1997. Precise point positioning for the efficient and robust analysis of GPS data from large networks, *J. Geophys. Res.*, 102(B3), 5005-5017.

Zwick, P., McCaffrey, R. and Abers, G., 1994. MT5 Program, In IASPEI Software Library, number 4, IASPEI.